Computational Materials Science 179 (2020) 109691

Contents lists available at ScienceDirect

Computational Materials Science

journal homepage: www.elsevier.com/locate/commatsci

Mechanical behaviors of MoS nanowires under tension from molecular dynamics simulations

Penghua Ying, Jin Zhang*, Jianli Zhou, Qixin Liang, Zheng Zhong*

School of Science, Harbin Institute of Technology, Shenzhen 518055, PR China

ARTICLE INFO

Keywords:
Nanowires
1D TMMs
Mechanical behavior
Molecular dynamics
Tensile test
Phase transformation

ABSTRACT

As a new class of one-dimensional (1D) transition-metal monochalcogenides (TMMs) nanowires (NWs), the recently synthesized MoS NWs exhibit potential applications in two-dimensional integrated circuit. However, their mechanical behaviors remain almost unexplored. In this paper, the mechanical behaviors of MoS NWs under tensile loading are studied by classical molecular dynamics simulations together with first-principles calculations. A novel phase transformation is observed in the MoS NWs when the strain applied to them is larger than a critical value, which results in tension-induced hardening in their tensile modulus. Due to the existence of phase transformation, a complicated mechanical response is observed in MoS NWs during the entire loading process, which successively experiences the linear, plateau, stress hardening and fracture stages. The influence of various factors including the strain rate and temperature on the mechanical properties of MoS NWs such as phase transformation, Young's modulus, fracture strength and fracture strain are also examined. The mechanical properties of MoS NWs obtained in this paper will be beneficial to their future applications in the semiconducting field. It is also expected that the results of the tension-induced phase transformation and its influence on the material properties observed in the present MoS NWs can be further extended to other 1D TMMs such as MoTe and SnSe NWs, since these 1D TMMs are found to possess the similar structure.

1. Introduction

The dimension of nanomaterials has a profound impact on their application prospects [1]. The two-dimensional (2D) materials especially the transition metal dichalcogenides (TMDs) and graphene have attracted intensive interests [2,3], due to the fact that their mechanical and physical properties are markedly different from those of their bulk counterparts. Similarly, one-dimensional (1D) NWs, dropping down one notch in dimensionality from 2D materials, have some unique properties, such as fewer defects, extremely high ratio of surface area to volume [4–6], quantum confinement [7–10], and effective strain relaxation [11–13]. The unique geometric configuration of NWs can be utilized as electronic device bases, such as channel and interconnect [14], which attracts massive attention in the field of semiconductor technology.

Recently, a new class of 1D nanomaterials namely the transition-metal monochalcogenides (TMMs) has been obtained from the TMDs through different physical [15,16,38] and chemical [1,17,18,39,40] methods. For instance, molybdenum-sulfide (Mo-S) crystals [19] such as the MoS [15,38] and Mo_5S_4 [16] NWs are mainly formed between holes created in a molybdenum disulfide (MoS_2) sheet under electron irradiation. Some other 1D crystals such as $NbSe_3$ [1], MoTe [17], SnSe [40], $HfTe_3$ [18] and HgTe [39] NWs are synthesized through a self-assembly chemical process, in which carbon nanotubes are used as molds to perform vapor-phase reaction [20]. Existing studies have shown that most Mo-S crystals are strongly bonded to the edge of 2D TMD sheets rather than simply weakly adhered to the surface, which makes them appealing in creating a 2D integrated circuit [15,16]. It is worth mentioning that although the synthesis method of MoTe, SnSe and MoS NWs is completely different, they possess the similar crystal structure, in which the Mo (Sn) and S (Te, Se) atoms are arranged in consecutive stacks of triangular layers rotated 180° along the axial direction of NWs [15,17,40]. Furthermore, different physical properties are observed in different Mo-S crystals. For example, Mo_5S_4 NWs are predicted to be semiconducting, while MoS NWs are metallic. Moreover, a unique self-adaptive torsional flexibility feature is found in MoS NWs [15,20], which shows promising applications for mechanical robust flexible electronics.

In addition to abundant synthesis methods have been proposed for 1D TMMs, some simulation studies recently have been reported on their material properties [15,16,20]. However, most studies are focused on the electrical properties of 1D TMMs and their mechanical behaviors

* Corresponding author.
E-mail addresses: jinzhang@hit.edu.cn (J. Zhang), zhongzheng@hit.edu.cn (Z. Zhong).

https://doi.org/10.1016/j.commatsci.2020.109691
Received 18 November 2019; Received in revised form 2 March 2020; Accepted 16 March 2020

remain almost unexplored. Although initial studies on the elastic modulus of the Mo-S (Mo_5S_4 and MoS) NWs has been conducted by first-principles calculations [16,44], this method cannot achieve a full understanding of the mechanical responses of NWs, since it cannot take into account the influence of finite temperature. Because the mechanics of NWs such as the fracture strength and fracture strain play an important role in the structural integrity and proper functioning of 1D TMMs in their application in interconnects of the 2D integrated circuit, it is thus necessary to conduct a comprehensive study on the mechanical behaviors of 1D TMMs.

In spite of the fact that most existing MoS NWs are found as a part of MoS_2 nanosheets, very recent research reported that the free-standing MoS NWs also can be synthesized through vapor-phase reactions in carbon nanotubes [40]. Hence, to promote the future applications of the very recently synthesized free-standing 1D TMMs, taking the free-standing MoS NWs as a typical example, in the present work we have investigate the mechanical behaviors of 1D TMMs by tensile tests through molecular dynamics (MD) simulations. Here, we choose the MoS NWs as a typical example because they have good potential applications in robust electronics and have a molecular structure analogous to most 1D TMM NWs. The mechanical properties such as Young's modulus, fracture strength and fracture strain of MoS NWs are examined. Specifically, a novel phase transformation is observed in MoS NWs under the tensile loading. The NWs exhibit a tension-induced hardening phenomenon in the novel phase.

2. Simulation methods

Fig. 1(a) shows the atomic structure of MoS NWs considered in recently experimental synthesis and characterization [15], which actually have a crystal structure same as Mo_5S_4 crystal considered in the previous first-principles calculations research [16]. In the present study the mechanical behaviors of MoS NWs were investigated by the tensile test, which is an experimental method widely employed to characterize the mechanical properties of various materials. Here, the tensile test was numerically implemented through MD simulations. In our MD simulations, MoS NWs were initially constructed based on the atomic structure observed from the experimental characterization [15]. As shown in Fig. 1(b), the lattice constants of the unit cell of the initially constructed NWs are 5.5 Å and 4.5 Å [4], respectively. The REBO potential [21,22] for Mo-S systems developed by Sinnottis [23] was used to describe the force interactions between atoms in our system. The whole process of MD simulations was carried out by the open-source simulation code LAMMPS [24], in which the standard Newton equations of motion were integrated in time using the velocity Verlet algorithm with a time step of 1 fs. To justify the reliability of the time step employed in our MD simulations, we checked the energy conservation of MoS NWs in NVE ensemble (constant atom number, volume, and energy). As shown in Fig. S1(a), during NVE simulations the total energy of NW keeps almost unchanged, which proves that the time step employed in our MD simulations is reasonable. The periodic boundary condition was applied along the axial direction, while the fixed boundary conditions were applied in other two directions. The size of the simulation box is 10 nm × 10 nm × 20 nm. The length of MoS NWs along the axial direction is 20 nm. A relatively large surface of 10 nm × 10 nm in the *x-y* plane was employed to ensure that there remains an enough place to allow the NWs to deform freely.

Since a correct molecular structure is of great importance in obtaining reliable results in MD simulations, the energy minimization and the structural relaxation were performed to obtain the stable configuration of MoS NWs before conducting the tensile test to them. Specifically, the energy minimization was performed by the conjugate gradient method. Afterwards, the system was relaxed at a certain temperature in the NPT ensemble (constant atom number, pressure, and temperature) with zero pressure applied in the axial direction. As a typical example, Fig. 1(d–f), respectively, show the changes of the total energy, the axial stress and the length of NWs under 0.1 K during the relaxation process. It is found that the values of total energy, length and

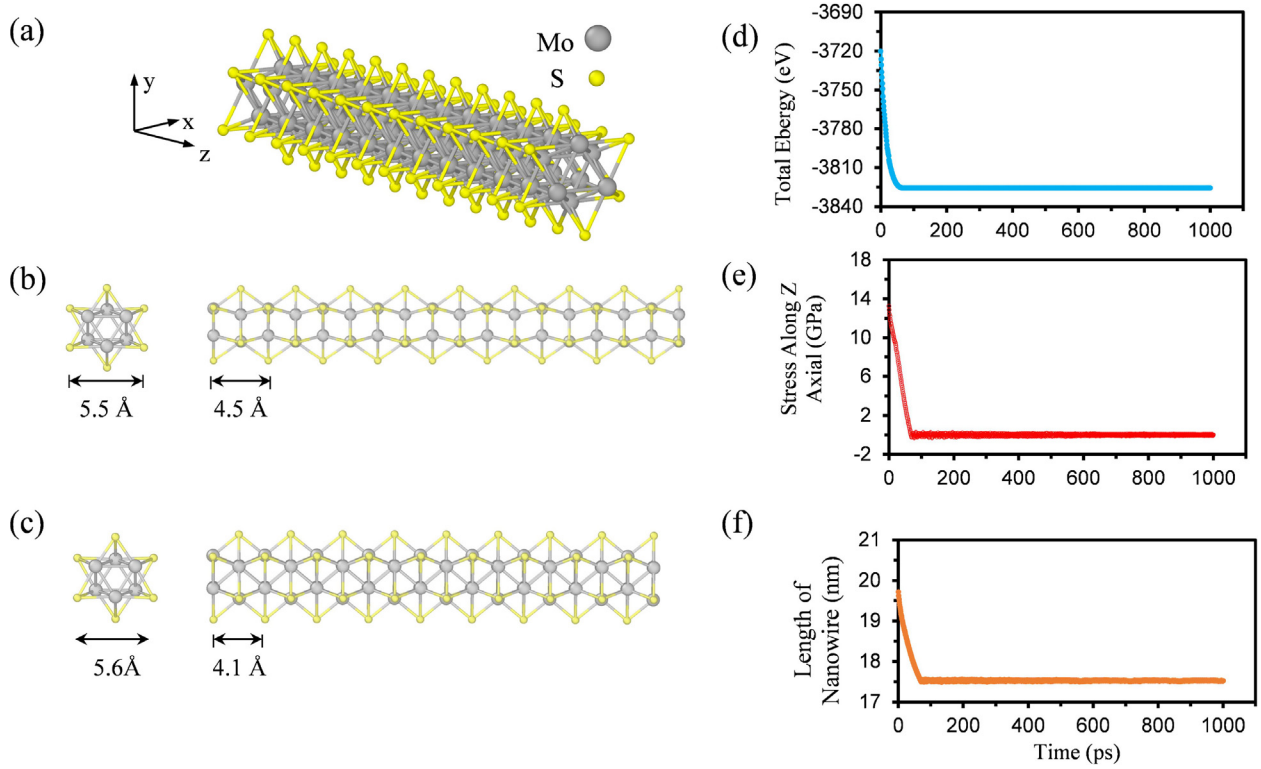

Fig. 1. Atomic structures of MoS NWs. (a) Perspective view of NWs. (b) The top view and side view of the initially constructed structure of NWs. (c) The top view and side view of NWs after energy minimization and structural relaxation. Changes in (d) the total energy, (e) the axial stress and (f) the length of NWs with running time during the structural relaxation process.

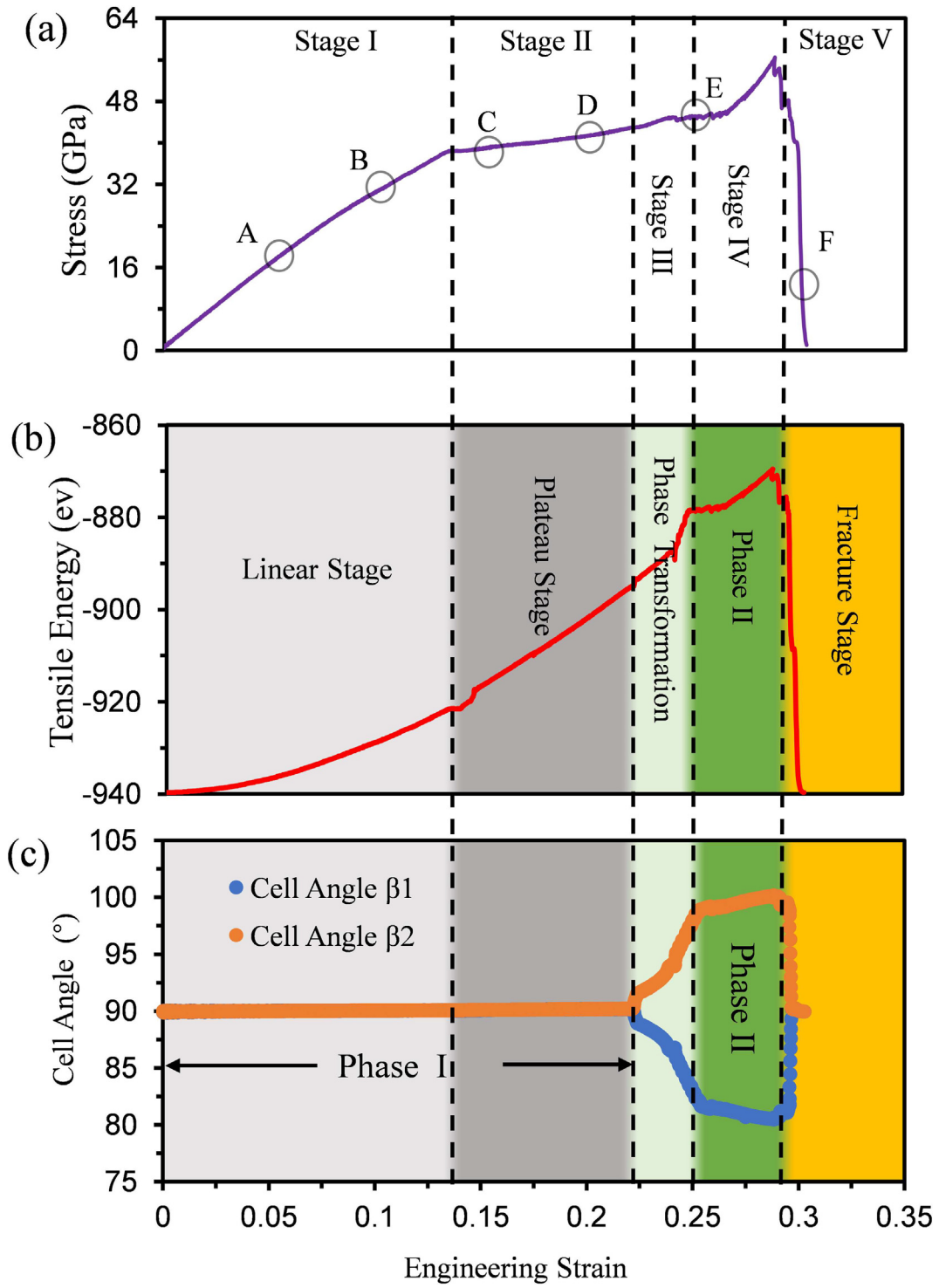

Fig. 2. Variation of (a) stress, (b) tensile energy and (c) cell angles of MoS NWs in different stages during the tensile test. Five stages are observed during the entire loading process: linear stage at strain 0 ~ 0.135, plateau stage at strain 0.135 ~ 0.22, phase transformation stage at strain 0.22 ~ 0.25, novel phase stage at strain 0.25 ~ 0.29, and fracture stage at strain greater than 0.29.

internal stress of NWs all keep falling in the initial 8×10^4 time steps (i.e., 80 ps). However, after 10^6 time steps (i.e., 1000 ps) the total energy and the length of NWs keep unchanged, corresponding to a nearly zero internal stress observed in NWs. This result indicates that the MoS NWs have approached their equilibrium state after 10^6 time steps. The obtained stable structure of MoS NWs is shown in Fig. 1(c). The lattice constant of the stable structure of MoS NWs is 5.6 Å in their x direction, which is exactly the same as the value 5.6 Å obtained from first-principles calculations [15]. The value of lattice constant in the z direction of MoS NWs is 4.1 Å, which is very close to the value 4.4 Å extracted from first-principles calculations and also the value 4.5 Å measured in experiments [15]. In terms of the lattice constant, a good agreement between the present MD simulations and the previous studies to some extent indicates that the REBO potential used in this study can appropriately describe the interactions between atoms in the MoS crystal.

After the energy minimization and structural relaxation processes, the MoS NWs were quasi-statically stretched along their axial direction with a constant engineering strain rate of 0.0001 ps^{-1} by increasing the periodic simulation box size in the tensile direction step-by-step. It should be noted that the tensile test simulation was implemented by alternately applying the strain to the NW and conducting the relaxation to the system. In other words, each 1 ps (1000 time steps) relaxation in NVT ensemble was performed after the simulation box was continuously expanded for 1 ps. Here, the engineering strain ε was defined as $\varepsilon = L - L_0/L$, where L and L_0 are lengths of NWs after and before the deformation, respectively. Meanwhile, the stress σ was calculated using the virial stress formulation, which is taken as the arithmetic mean of the local stresses on all atoms and has the following expression: [25]

$$\sigma = \frac{1}{V}\sum_{i=1}^{N}\left(m_i v_a^i v_a^i + \frac{1}{2}\sum_{j\neq 1}^{N} F_a^{ij} r_a^{ij}\right) \quad (1)$$

where V and N are the volume and the total atom number of the system; m_i and v_a^idenote the mass and the axial velocity of atom i; $F_a^{ij}$and r_a^{ij}represent the force and the distance between atoms i and j in the axial direction. In calculating the volume V of MoS NWs, the NW was assumed to be a cylinder [26] with a radius of 3 Å, which equals to the distance between the centroid and exterior surface sulfur atoms. More details of the volume calculation can be found in Fig. S2 (see the Supplementary Material).

The first-principles calculations, which were conducted to calculate the stress, energy and band structure of MoS crystals, were implemented by density functional theory calculations with the aid of the CASTEP package together with the generalized gradient approximation of the Perdew-Burke-Ernzerhof functional form [41]. A 381 eV cutoff for the plane wave basis set was adopted in all calculations. The reliability of the selected cutoff was proven by the fact that, as shown in Fig. S1(b), the tensile behviours of NWs almost unchange with continuously increasing cutoff. Moreover, The convergence threshold employed in the present density functional theory calculations was set as 10^{-6} eV in energy and 10^{-3} eV/Å in force. A vacuum space of 200 Å was used in both x and y directions to avoid interactions between adjacent layers. In caculating the band structures, the Brillouin zone was sampled with a 6 × 6 × 2 Γ-centered Monkhorst-Pack [42] K-points grid.

3. Results and discussions

In this section, the aforementioned tensile MD simulations together with the first principle calculations were employed to study the mechanical behaviors of MoS NWs. the effects of temperature and strain rate on the tensile properties of MoS NWs were examined.

3.1. Mechanical responses under tensile loading

In Fig. 2(a) and (b) we show the stress–strain and energy-strain relationships of MoS NWs under the tensile loading. Here, the MoS NWs under 0.1 K is shown an example. It is known that, at a temperature near absolute zero the influence of thermal fluctuation can be almost totally excluded. Thus, the models under 0.1 K can serve as a necessary first step towards understanding the major factors affecting the mechanical behaviors of MoS NWs subject to tensile loading. The effect of temperature will be discussed later. Configurations of the NW at points A to F in Fig. 2(a) are shown in Fig. S3 (see the Supplementary Material). During the entire tensile loading process, it is found that the NWs firstly elongate without obvious structural change at strains initially varying from 0 to 0.2. However, when the applied strain increases to the value between 0.2 and 0.25, the phase transformation occurs, resulting in a topological change in the geometry of the NWs. As shown Fig. 2(c), the unit cell in the MoS NWs is always vertical to the NW axial axis before the phase transformation, irrespective to the external loading. However, an inclination is observed in the unit cell after the phase transformation, which will be discussed in details later. According to the changes of cell angles defined in Fig. S4 (see the Supplementary Material), the total loading process can be divided into four stages as shown in Fig. 2c, which successively are the elastic deformation stage within parent phase (noted as phase I), the phase transformation stage, the stress hardening stage within transformed phase (noted as phase II) and the final fracture stage.

Moreover, it can be seen from Fig. 2 that even prior to the occurrence of the phase transformation, the loading responses of NWs exhibit two different stages. When the strain is between 0 and 0.135, the MoS NWs experience the linear elastic deformation. In this stage the stress significantly increases with growing strain. If we keep increasing the strain, i.e., a strain between 0.135 and 0.22, the stress–strain relationship changes in the NWs. In the plateau stage, although the stress still almost linearly increases with the increasing strain, the growing rate is significantly reduced. Under this circumstance, the total elastic deformation stage within the parent phase can be further divided into the linear stage and the plateau stage, which results in five stages (see Fig. 2(a) and 2(b)) during whole loading process. It can be found that the stress in the NWs within the new phase II grows more and more rapidly with growing strains, which indicates that the elastic modulus of the new phase increases as the applied strain increases. This stress hardening phenomenon will be discussed in details later. After the phase II stage, if we keep stretching the NWs, a fracture failure occurs. The fracture strain and the fracture strength obtained from Fig. 2(a) and (b) are 0.29 and 56.4 GPa, respectively. In Fig. 3 we show the elastic modulus of MoS NWs. Here two methods are employed to calculate the elastic modulus. The first method is calculating the elastic modulus from the stress–strain relationship. From the stress–strain curve, the elastic modulus E can be obtained through $E = \Delta\sigma/\Delta\varepsilon$, where $\Delta\varepsilon$ is the increment in strain and $\Delta\sigma$ is the corresponding increment in stress. The second method is from the energy-strain relationship, based on which the elastic modulus can be defined as $E = \partial^2 U/\partial\varepsilon^2$ with U being the potential energy density. It is noted that, to satisfy the assumption of linear elasticity, the elastic modulus is calculated by from the stress–-strain and energy-strain curves under $\varepsilon < 0.05$. As shown in Fig. 3(a), the elastic moduli extracted from the stress–strain and energy-strain curves are 324.9 GPa and 294.8 GPa, respectively, which are close to each other. This discrepancy can be attributed to the fact that only the axial stress was accounted in the stress–strain curves, while other effects like shear contributions were included in the energy-strain curves [26]. The elastic modulus of MoS NWs is much larger than that of single-layer MoS_2 sheets (200–230 GPa) [30], MoS_2 nanotube (211.1–220 GPa) [29] and significantly smaller than that of carbon allotropes, such as the CNT (1TPa) [43] and diamond nanothreads (850GPa) [26].

It is shown in the previous studies [27–29] that the cutoff function in the REBO potential can overestimate the necessary forces for breaking covalent bonds through the unphysical increasing of forces for bonds within the cutoff region. Thus, it is necessary to verify the reliability of the fracture behaviors by some other means. Here, as shown in Fig. S6 (see the Supplementary Material), we calculated the stress–strain relationship of MoS NWs through first-principles calculations. The fracture strain obtained from first-principles calculations is between 0.25 and 0.35, while the fracture strength is 55.7 GPa. The calculated fracture strain and strength are consistent with the results extracted from MD simulations, which further proves that the REBO potential can reliably describe the mechanical behaviors of MoS NWs under tension.

Fig. 3(b) shows the tangent modulus of the MoS NWs, each of which is obtained by applying the linear curve fitting to the stress–strain data per 50 ps at different stages. The tangent modulus is around 269.8 GPa at the linear stage and then drops to a value around 55.6 GPa at the plateau stage. At the phase transformation stage, a significant fluctuation is found in the value of tangent modulus. Surprisingly, with

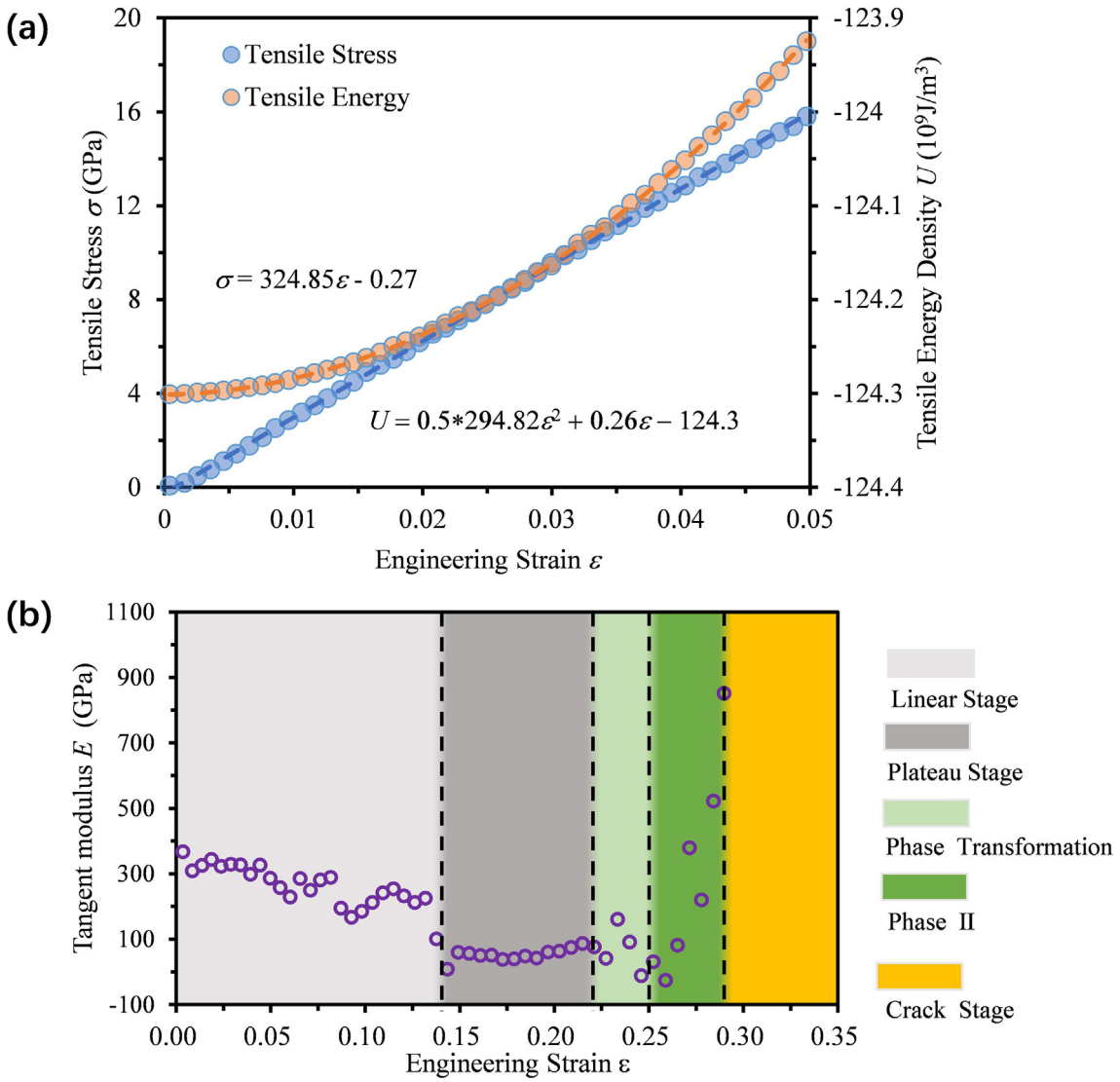

Fig. 3. (a) The elastic modulus of MoS NWs obtained from their stress–strain and energy-strain relationships under a small strain 0–0.05. (b) The tangent modulus of MoS NWs at different stages.

increasing tensile strain the modulus of NWs within new phase II increases from 30.8 GPa to 851.4 GPa, which indicates that the new phase of MoS NWs exhibits a strong tension-induced hardening phenomenon.

The phase transformation also results in an energy reduction of MoS NWs. As illustrated in Fig. S5 (extracted from Fig. 2(b) and (c)), an energy reduction is observed when the strain is around 0.243 in the phase transformation stage. The strain reduction corresponds to the change of cell angle after the phase transformation. However, the energy reduction induced by the phase transformation is relatively small, which can be attributed to the fact that the phase transformation only changes the cell angle without other obvious structural changes. In Fig. S7 (see the Supplementary Material) the relative energy in parent phase I and transformed phase II is plotted when the MoS NWs are subjected to different tensile strains along the axial direction. Here, the relative energy is obtained by first-principles calculations. Expect for phase II under a strain larger than 0.22, all unit cells utilized in first-principles calculations are extracted from the above MD simulations. The unit cell of phase I under a strain larger than 0.22 is obtained by directly expanding the axial length of the unit cell of NWs in first-principles calculations. It is found very clearly that the relative energy of the transformed phase (phase II) is smaller than that of its parent counterpart (phase I), which indicates that the transformed phase of MoS NWs is more energetically favorable than the parent phase. This fact further proves the phase transformation phenomenon of the MoS NWs observed in the above MD simulations.

3.2. Structural evolution

In Figsures 2(c), 4 and 5 we show the changes of cell angles, bond lengths and bond angles between two neighboring planes in the unit cell, respectively, which are helpful in achieving a clearer understanding of the structural changes in the NWs at different stages. Specifically, as shown in Fig. 2(c), in order to know more accurately the critical strain corresponding to the onset of the phase transformation, two cell angles β_1 and β_2 between the unit cell and the NW axial axis are defined (see Fig. S4 in the Supplementary Material). In Fig. 2(c) we show the changes in the cell angles β_1 and β_2 with respect to the applied axial strain ε during the whole tensile process. It is found that both cell angles keep around 90° until the strain reaches 0.22. After that, when the strain grows to a value ranging between 0.22 and 0.25, β_1 drops rapidly from 90° to 82.9°, while β_2 rises rapidly from 90° to 97.9°, rotating within the direction opposite to β_1. The significant change in cell angles proves the occurrence of the phase transformation in the stretched MoS NWs. When the strain is larger than 0.25 but < 0.29, the

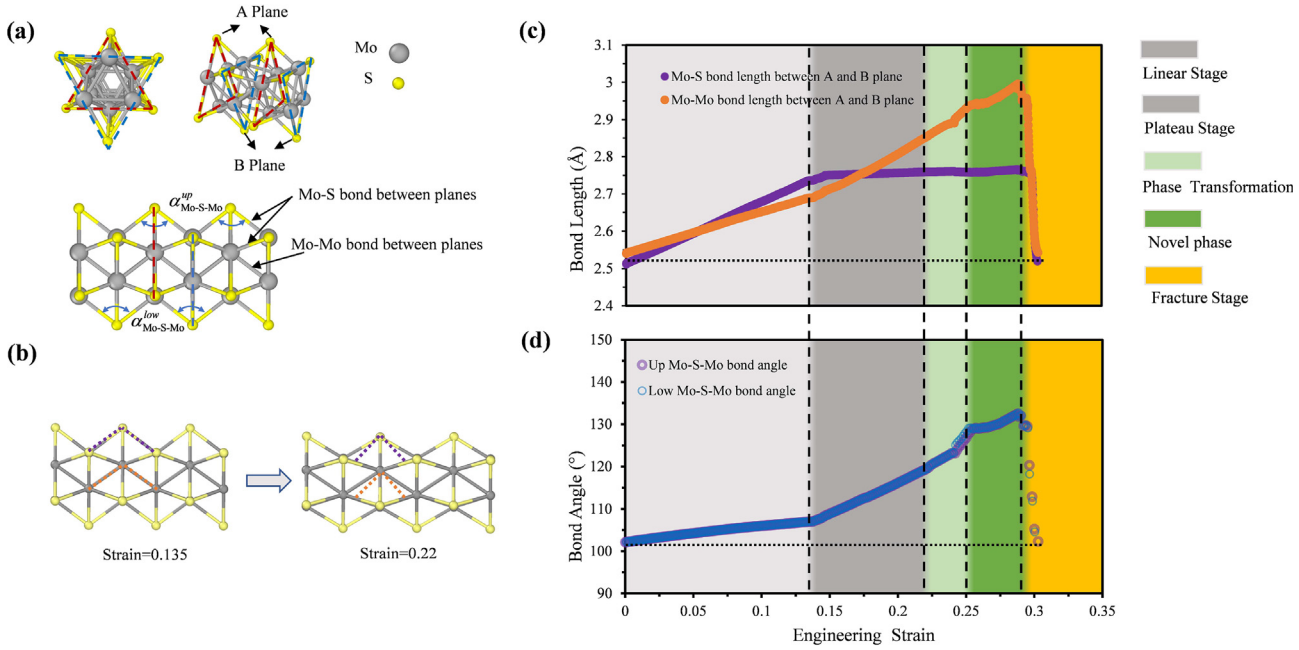

Fig. 4. Changes of bond length and bond angle between A and B planes during the entire loading process. (a) Definitions of A and B planes, Mo-S bonds, Mo-Mo bonds, top Mo-S-Mo bond angles and bottom Mo-S-Mo bond angles at a unit cell. (b) Configuration changes of MoS NWs at the beginning and end of the plateau stage. (c) Changes of bond lengths and (d) changes of bond angles between A and B planes against strain.

changing rate of cell angles becomes slow. For example, at this loading stage the cell angle β_1 drops from 82.9° to 80.6°, while β_2 rises from 97.9° to 100°. The changes in cell angles are consistent with the previously observed configuration changes of MoS NWs (see Figs. S1 and S2), which proves that a new phase has been produced at this stage. When the strain is more than 0.29, both cell angles recover to 90° due to the axial stress release caused by the final fracture of MoS NWs.

Fig. 4 shows the average bond length distribution of MoS NWs with different strains in their axial direction. It is found that the length of both Mo-S and Mo-Mo bonds firstly increases with the increasing strain at the linear stage ($0 < \varepsilon < 0.135$). At the plateau stage ($0.135 < \varepsilon < 0.22$), with increasing the strain the Mo-Mo bond length keeps increasing within a larger growing rate, while the Mo-S bond length almost keeps unchanged. A similar phenomenon is also found in both phase transformation stage ($0.22 < \varepsilon < 0.25$) and stress hardening stage within phase II ($0.25 < \varepsilon < 0.29$). At the final stage ($\varepsilon$ greater than 0.29), the fracture failure occurs accompanying with a release of the stress, which results in the recovery of the bond length to its initial value. In Fig. 4(d) we show the average value of the top and bottom Mo-S-Mo bond angles in MoS NWs under different tensile strains. The values of these two bond angles are almost identical to each other, which means that A and B planes keep parallel during the entire loading process. The Mo-S-Mo bond angle increases slowly at the initial linear stage and then transforms to a sharp increase at the following plateau stage, phase transformation and novel phase stages. This indicates that at the linear stage the elongation of NWs is mainly attributed to the increase of Mo-S and Mo-Mo bonds, while at the subsequent stages the increase of Mo-S-Mo bond angles turns to play the dominate role in the elongation of NWs. Specifically, it is noted that at the plateau stage, the Mo-Mo bond length continues to increase, while the Mo-S bond length remains unchanged. As a result, at this stage the Mo atom and the S atom tend to lie in different planes, which may lead to the tilt of the unit cell and thereby cause a new phase. Moreover, there is some disturbance in the change of bond lengths and bond angles at the phase transformation stage, which is attributed to the continuous change of MoS NW structures during the phase transition process.

Fig. 5 shows the changes of the in-plane bond length against the strain at different stages. The Mo-S bond together with the horizontal and oblique Mo-Mo bonds is denoted in Fig. 5(a). It is noted that the distributions of the average bond length in two neighboring planes are almost the same. The length of Mo-S bonds is found to drop very slowly at the linear stage, but the dropping rate is greatly increased at the subsequent stages prior to its final fracture (see Fig. 5(b)). The changes of Mo-Mo bonds illustrated in Fig. 5(c), however, show a different changing trend. The length of both oblique and horizontal Mo-Mo bonds drops firstly at the linear stage but then turns to increase at the plateau stage. When the NW enters the phase transformation stage, two branches are observed in the changing path at $0.24 < \varepsilon < 0.25$. The length of oblique Mo-Mo bonds continues to increase with a larger growing rate, while a drop is found in their horizontal counterparts. At the novel phase stage, the length of the oblique Mo-Mo bonds keeps increasing, while their horizontal counterparts keep almost unchanged. These different changing trends observed between two kinds of Mo-Mo bonds are consistent with the rapid structural change in the phase transformation process. The length of both oblique and horizontal Mo-Mo bonds recovers to its initial value after the fracture happens. The decrease of bond length observed in both Mo-Mo and Mo-S bonds during the linear stage is due to the in-plane compression caused by inter-plane stretching. As mentioned before, at the plateau stage, the elongation of MoS NWs is mainly caused by the increase of their inter-plane bond angels (see Fig. 4(b)) rather than the increase of inter-plane bond lengths. However, different changing trends of inter-plane Mo-Mo and Mo-S bond lengths induce the different distribution of in-plane Mo-Mo and Mo-S bond lengths against strain at the subsequent stages.

To explain why the elastic modulus becomes small at the plateau stage, we show the changes in the bond length and bond angle of MoS NWs in Fig. 6(a). It should be noted that the bond length and angle calculations were averaged in the region far from the cracks. It is clearly shown in Fig. 6(a) that the reduced elastic modulus at the plateau stage is mainly due to the elongation of NWs at this stage, which is mainly induced by the change of Mo-S-Mo bond angle between neighboring planes rather than the change of the inter-planes bond length observed at the linear stage. During the phase transformation, as shown in Fig. 6(b), the in-plane Mo-S bond is compressed due to the increase of the inter-plane Mo-S bond length (marked as blue lines) and also the

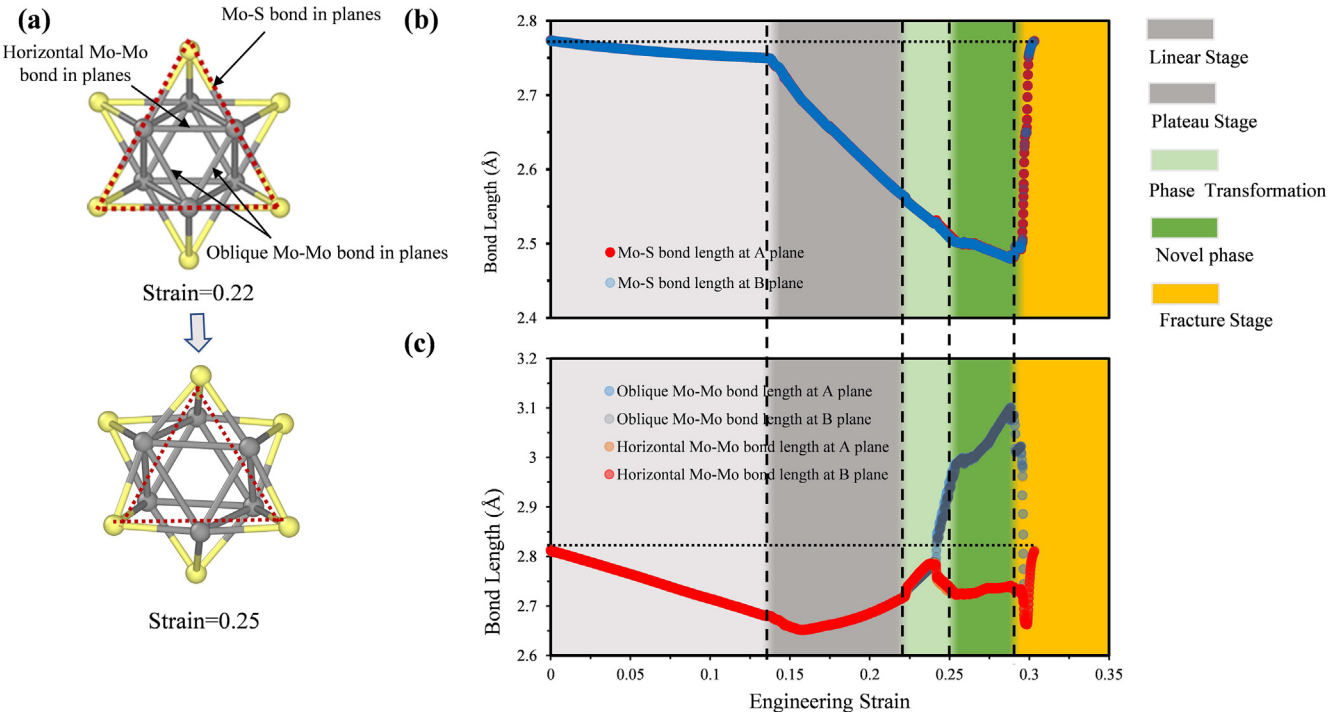

Fig. 5. Changes of bond length in A and B planes during the entire loading process. (a) Configuration changes of MoS NWs at the beginning and end of the phase transformation stage. (b) Changes of in-plane Mo-S bond length and (c) changes of in-plane Mo-Mo bond length against the strain.

Mo-S-Mo bond angle under tensile loading. Specifically, when the compression in the in-plane Mo-S bonds is relatively large, the in-plane Mo-S bonds (marked as red lines) tend to lose stability as shown in Fig. 6(b). As a result, the center Mo atom move leftward, while the crystal further begins to incline. This process sustains till the end of the phase transformation and thus is the major reason causing the tension-induced phase transformation in MoS NWs. After the phase transformation, although the changing rate of cell angles becomes slow, the inclination still keeps ongoing in the unit cell of MoS NWs (see Fig. 2(c)), which may cause the densification of the NW structure. In response to this densification process, the elastic modulus continues to increase with increasing strain during the phase transformation.

3.3. Temperature and strain rate effects

Next, we study the effects of temperature and strain rate on the

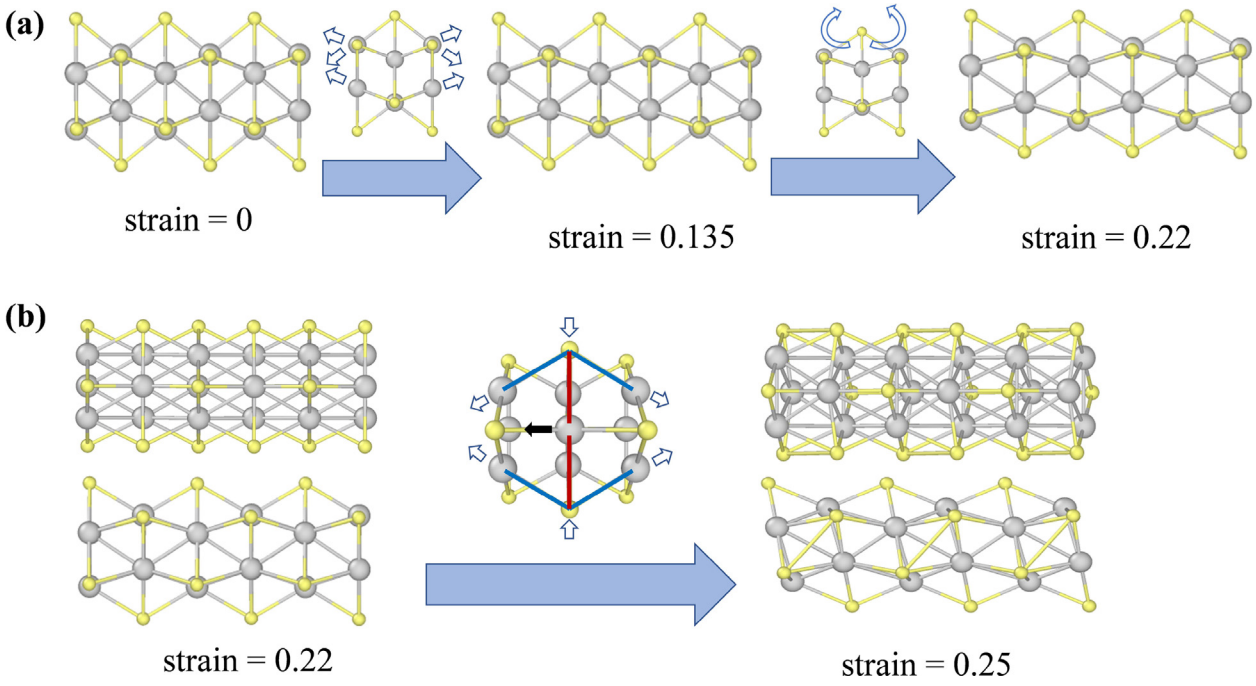

Fig. 6. The deformation schematic of MoS NWs under tensile loading. (a) The linear stage and plateau stage. (b) Phase transformation, where (b1) the crystal structure of phase I ($\varepsilon = 0$) before phase transformation, (b2) during phase transformation, and (b3) phase II ($\varepsilon = 0.25$) after phase transformation. It is noted that to show the phase transformation mechanism more clearly the Mo-Mo bond is not drawn here and the perspective view is used in (b2).

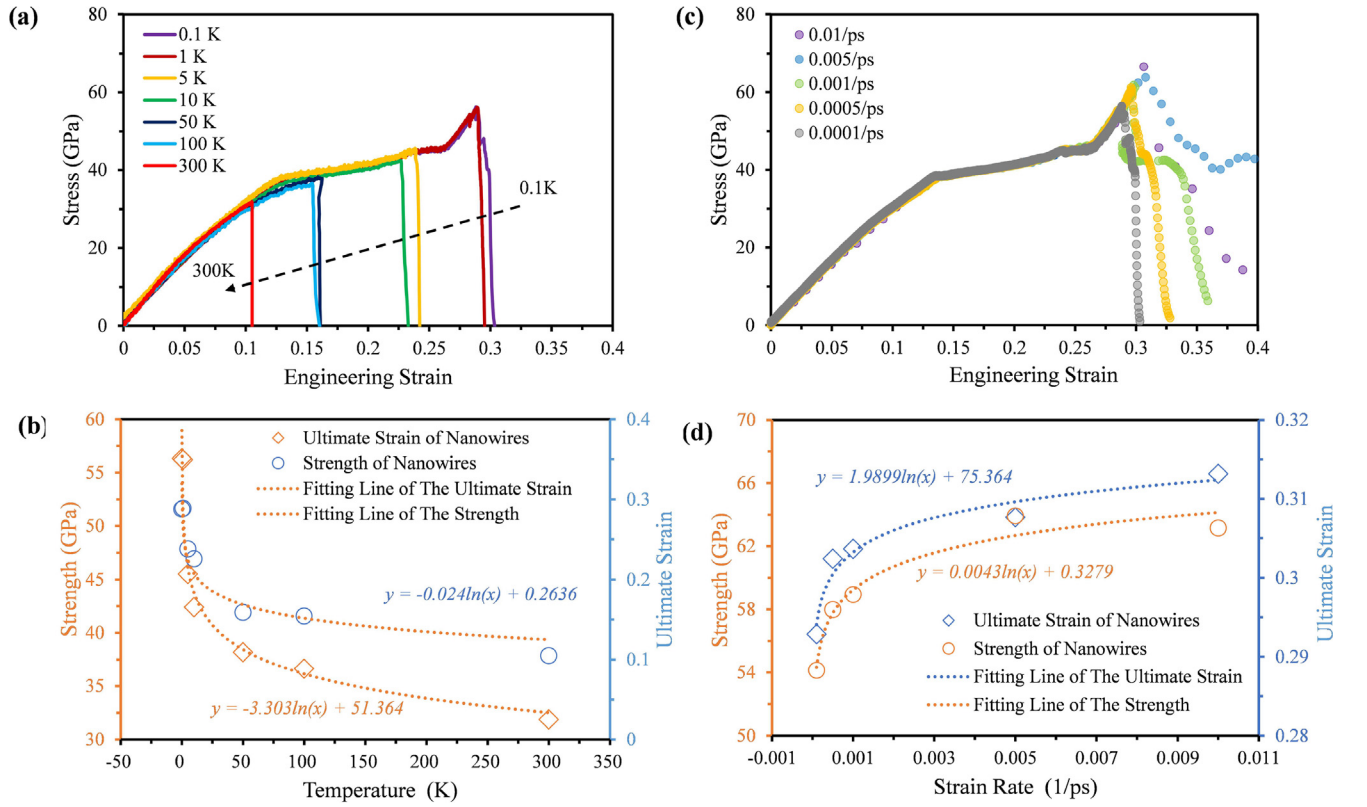

Fig. 7. The mechanical response of MoS NWs under tension at different temperatures and strain rates. (a) Stress–strain relationships under different temperatures. Here the strain rate is set as 0.0001 ps-1. (b) Fracture strength and fracture strain under different temperatures. (c) Stress–strain relationships at different strain rates. Here the temperature is set as 0.1 K. (d) Fracture strength and fracture strain at different strain rates.

mechanical properties of MoS NWs. In the study of the temperature effect, MD simulations are performed at a fixed strain rate of 0.0001 ps^{-1} but under different temperatures ranging from 0.1 K to 300 K. To study the influence of strain rate, a constant temperature of 0.1 K is selected, while the strain rate is changed from 0.0001 ps^{-1} to 0.01 ps^{-1}. The simulated stress–strain curves at different temperatures are shown in Fig. 7(a) for NWs under the tensile loading along the axial directions. It can be found that the temperature has a strong influence on the fracture strength and fracture strain, while the stress–strain curves of NWs under different temperatures are coincident with each other at a small strain ($0 < \varepsilon < 0.05$), which means that the elastic modulus is almost independent of temperature. However, the temperature is found to significantly affect the mechanical responses of NWs after the linear stage. As for MoS NWs under 0.1 K and 1 K, all five stages as we illustrated above are observed. Only the linear stage and the plateau stage are observed in the MoS NWs under 5 K and 10 K. Eventually, the fracture failure is found in the NWs under 50 K and 100 K just after they enter the plateau stage. However, when the temperature rises to the room temperature 300 K, the fracture of MoS NWs occurs in the linear stage. This result indicates that the novel phase will occur in the MoS NWs under a relatively low temperature (at least < 5 K). Unlike the temperature effect, the strain rate has a trivial effect on the stress–strain curves as shown in Fig. 7(c). All stages including the phase transformation are observed in NWs loaded with different strain rates. The stress–strain curves of MoS NWs loaded with different strain rates are highly coincident with each other before their fracture. Based on the stress–strain curves obtained from MD simulations, the fracture strength and fracture strain of NWs under different temperatures and with different strain rates are plotted in Fig. 7(b) and 7(d), respectively. It is found that, although the fracture strength and fracture strain drop against the temperature and increase against the strain rate, the temperature-dependent and strain rate-dependent fracture strength (fracture strain) of MoS NWs can be described by the same logarithmic equation as shown below

$$A = a\ln(B) + b \tag{2}$$

where $A \in (\sigma_T, \varepsilon_{max})$ with σ_T and ε_{max} being the fracture strength and fracture strain, respectively. $B \in (T, \dot{\varepsilon})$, where T and $\dot{\varepsilon}$denote the temperature and strain rate, respectively. a and b are constants which need to be fitted from the curves as shown in Fig. 7(b) and (d).

In the above discussion, we find that due to the changes in the MoS NW structure after the phase transformation, the elastic moduli extracted from stress-strain curves before and after phase transformation are quite different. In the previous studies, the bandgap engineering is often implemented through applying a strain to change the crystal structure of nanomaterials [13,31–37]. It is thus of great interest to figure out whether the phase transformation can trigger similar changes in the electronic properties of MoS NWs just like that on their mechanical properties. Motivated by this idea, the electronic band structures of MoS NWs within phase I and phase II are calculated by first-principles calculations. As shown in Fig. S8 (see the Supplementary Material), the MoS NWs are found to have no band gaps in both phases, which indicates that the MoS NWs show a metallic characteristic during the whole loading process and their electronic properties keep stable under tensile loading. This fact further demonstrates that the MoS NWs can serve as a flexible metallic component to connect the semiconducting TMD monolayers in the future applications.

4. Conclusions

The mechanical behaviors of MoS NWs under the tensile loading are comprehensively investigated in this paper by classical MD simulations together with first-principles calculations. A complicated mechanical response is observed in MoS NWs under tensile loading, which

successively experience the linear, plateau, stress hardening and fracture stages. The mechanical properties such as Young's modulus, fracture strength and fracture strain of MoS NWs are achieved. These mechanical properties of MoS NWs are also found to be strongly dependent on temperature but be trivially sensitive to the strain rate. Configurations including bond lengths and bond angles of MoS NWs under different strains are well examined to explain the mechanical responses of MoS NWs under different loading stages. It is found that when the applied strain is larger than a critical value, a novel phase transformation is observed in the MoS NWs under an extremely low temperature, which is responsible for the stress hardening phenomenon observed in MoS NWs during the loading process.

CRediT authorship contribution statement

Penghua Ying: Conceptualization, Methodology, Investigation, Formal analysis, Writing - original draft, Writing - review & editing. **Jin Zhang:** Conceptualization, Formal analysis, Writing - review & editing. **Jianli Zhou:** Software, Formal analysis. **Qixin Liang:** Data curation, Formal analysis. **Zheng Zhong:** Resources, Writing - review & editing, Supervision, Project administration, Funding acquisition.

Declaration of Competing Interest

The authors declare that they have no known competing financial interests or personal relationships that could have appeared to influence the work reported in this paper.

Acknowledgements

This study was supported by the National Key R&D Program of China (No. 2018YFB1502600) and the National Natural Science Foundation of China (Nos. 11932005, 11772106).

Data availability

The raw data required to reproduce these findings are available. The processed data required to reproduce these findings are also available.

Appendix A. Supplementary data

Supplementary data to this article can be found online at https://doi.org/10.1016/j.commatsci.2020.109691.

References

[1] T. Pham, S. Oh, P. Stetz, et al., Torsional instability in the single-chain limit of a transition metal trichalcogenide, Science 361 (6399) (2018) 263–266.
[2] J. Zhou, J. Lin, X. Huang, et al., A library of atomically thin metal chalcogenides, Nature 556 (7701) (2018) 355.
[3] Y. Han, M.Y. Li, G.S. Jung, et al., Sub-nanometre channels embedded in two-dimensional materials, Nat. Mater. 17 (2) (2018) 129.
[4] J. Li, W. Wan, H. Zhou, et al., Hydrothermal synthesis of TiO_2 (B) nanowires with ultrahigh surface area and their fast charging and discharging properties in Li-ion batteries, Chem. Commun. 47 (12) (2011) 3439–3441.
[5] X. Wen, S. Wang, Y. Ding, et al., Controlled growth of large-area, uniform, vertically aligned arrays of α-Fe_2O_3 nanobelts and nanowires, J. Phys. Chem. B 109 (1) (2005) 215–220.
[6] H. Liang, M. Upmanyu, H. Huang, Size-dependent elasticity of nanowires: nonlinear effects, Phys. Rev. B 71 (24) (2005) 241403.
[7] X. Zhao, C.M. Wei, L. Yang, et al., Quantum confinement and electronic properties of silicon nanowires, Phys. Rev. Lett. 92 (23) (2004) 236805.
[8] M. Bruno, M. Palummo, A. Marini, et al., Excitons in germanium nanowires: Quantum confinement, orientation, and anisotropy effects within a first-principles approach, Phys. Rev. B 72 (15) (2005) 153310.
[9] M.R. Black, Y.M. Lin, S.B. Cronin, et al., Infrared absorption in bismuth nanowires resulting from quantum confinement, Phys. Rev. B 65 (19) (2002) 195417.
[10] K. Pemasiri, M. Montazeri, R. Gass, et al., Carrier dynamics and quantum confinement in type II ZB-WZ InP nanowire homostructures, Nano Lett. 9 (2) (2009) 648–654.
[11] I.A. Goldthorpe, A.F. Marshall, P.C. McIntyre, Synthesis and strain relaxation of Ge-core/Si-shell nanowire arrays, Nano Lett. 8 (11) (2008) 4081–4086.
[12] F. Glas, Critical dimensions for the plastic relaxation of strained axial heterostructures in free-standing nanowires, Phys. Rev. B 74 (12) (2006) 121302.
[13] H.J. Xiang, S.H. Wei, J.L.F. Da Silva, et al., Strain relaxation and band-gap tunability in ternary $In_xGa_{1-x}N$ nanowires, Phys. Rev. B 78 (19) (2008) 193301.
[14] Nanowires: Recent Advances. BoD–Books on Demand, 2012.
[15] J. Lin, O. Cretu, W. Zhou, et al., Flexible metallic nanowires with self-adaptive contacts to semiconducting transition-metal dichalcogenide monolayers, Nat. Nanotechnol. 9 (6) (2014) 436.
[16] X. Liu, T. Xu, X. Wu, et al., Top–down fabrication of sub-nanometre semiconducting nanoribbons derived from molybdenum disulfide sheets, Nat. Commun. 4 (2013) 1776.
[17] M. Nagata, S. Shukula, Y. Nakanishi, et al., Isolation of single-wired transition-metal monochalcogenides by carbon nanotubes, Nano Lett. (2019).
[18] S. Meyer, et al., Metal-insulator transition in quasi-one-dimensional $HfTe_3$ in the few-chain limit, Phys. Rev. B 100 (4) (2019) 041403.
[19] P. Murugan, V. Kumar, Y. Kawazoe, et al., Assembling nanowires from Mo−S clusters and effects of iodine doping on electronic structure, Nano Lett. 7 (8) (2007) 2214–2219.
[20] A.L. Koh, S. Wang, C. Ataca, et al., Torsional deformations in subnanometer MoS interconnecting wires, Nano Lett. 16 (2) (2016) 1210–1217.
[21] D.W. Brenner, Empirical potential for hydrocarbons for use in simulating the chemical vapor deposition of diamond films, Phys. Rev. B 42 (15) (1990) 9458.
[22] D.W. Brenner, O.A. Shenderova, J.A. Harrison, et al., A second-generation reactive empirical bond order (REBO) potential energy expression for hydrocarbons, J. Phys. Condens. Matter 14 (4) (2002) 783.
[23] T. Liang, S.R. Phillpot, S.B. Sinnott, Parametrization of a reactive many-body potential for Mo–S systems, Phys. Rev. B 79 (24) (2009) 245110.
[24] S. Plimpton, Fast parallel algorithms for short-range molecular dynamics, J. Comput. Phys. 117 (1) (1995) 1–19.
[25] J.A. Zimmerman, E.B. WebbIII, J.J. Hoyt, et al., Calculation of stress in atomistic simulation, Modell. Simul. Mater. Sci. Eng. 12 (4) (2004) S319.
[26] R.E. Roman, et al., Mechanical properties and defect sensitivity of diamond nanothreads, Nano Lett. 15 (3) (2015) 1585–1590.
[27] O.A. Shenderova, D.W. Brenner, A. Omeltchenko, et al., Atomistic modeling of the fracture of polycrystalline diamond, Phys. Rev. B 61 (6) (2000) 3877.
[28] H. Zhan, G. Zhang, V.B.C. Tan, et al., From brittle to ductile: a structure dependent ductility of diamond nanothread, Nanoscale 8 (21) (2016) 11177–11184.
[29] E.W. Bucholz, S.B. Sinnott, Mechanical behavior of MoS_2 nanotubes under compression, tension, and torsion from molecular dynamics simulations, J. Appl. Phys. 112 (12) (2012) 123510.
[30] J.W. Jiang, H.S. Park, T. Rabczuk, Molecular dynamics simulations of single-layer molybdenum disulphide (MoS_2): Stillinger-Weber parametrization, mechanical properties, and thermal conductivity, J. Appl. Phys. 114 (6) (2013) 064307.
[31] H.J. Conley, B. Wang, J.I. Ziegler, et al., Bandgap engineering of strained monolayer and bilayer MoS_2, Nano Lett. 13 (8) (2013) 3626–3630.
[32] A. Maiti, Carbon nanotubes: Bandgap engineering with strain, Nat. Mater. 2 (7) (2003) 440.
[33] B. Sa, Y.L. Li, J. Qi, et al., Strain engineering for phosphorene: the potential application as a photocatalyst, J. Phys. Chem. C 118 (46) (2014) 26560–26568.
[34] S.B. Desai, G. Seol, J.S. Kang, et al., Strain-induced indirect to direct bandgap transition in multilayer WSe_2, Nano Lett. 14 (8) (2014) 4592–4597.
[35] J. Qi, X. Qian, L. Qi, et al., Strain-engineering of band gaps in piezoelectric boron nitride nanoribbons, Nano Lett. 12 (3) (2012) 1224–1228.
[36] H. Bao, Y. Huang, Z. Yang, et al., Tensile loading induced phase transition and rippling in single-layer MoS_2, Appl. Surf. Sci. 404 (2017) 180–187.
[37] J. Zhang, Phase transformation in two-dimensional covalent organic frameworks under compressive loading, PCCP 20 (46) (2018) 29462–29471.
[38] W. Huang, et al., In-situ fabrication of Mo_6S_6-nanowire-terminated edges in monolayer molybdenum disulfide, Nano Res. 11 (11) (2018) 5849–5857.
[39] J.H. Spencer, et al., Raman spectroscopy of optical transitions and vibrational energies of ~1 nm HgTe extreme nanowires within single walled carbon nanotubes, ACS Nano 8 (9) (2014) 9044–9052.
[40] C.A. Slade, et al., Unprecedented new crystalline forms of snse in narrow to medium diameter carbon nanotubes, Nano Lett. 19 (5) (2019) 2979–2984.
[41] J.P. Perdew, K. Burke, M. Ernzerhof, et al., Generalized gradient approximation made simple, Phys. Rev. Lett. 77 (18) (1996) 3865–3868.
[42] H.J. Monkhorst, J.D. Pack, Special points for Brillouin-zone integrations, Phys. Rev. B 13 (12) (1976) 5188–5192.
[43] W.X. Bao, C.C. Zhu, W.Z. Cui, Simulation of Young's modulus of single-walled carbon nanotubes by molecular dynamics, Physica B Conden. Matter. 352 (1–4) (2004) 156–163.
[44] Daniel F. Souza, Andréia L. Rosa, Pedro Venezuela, José E. Padilha, Adalberto Fazzio, Renato B. Pontes, Structural evolution and the role of native defects in subnanometer MoS nanowires, Phys. Rev. B 100 (23) (2019) 235416(8).